PHYSICAL REVIEW C **94**, 054007 (2016)

# Local chiral potentials with Δ-intermediate states and the structure of light nuclei

M. Piarulli,[1] L. Girlanda,[2,3] R. Schiavilla,[4,5] A. Kievsky,[6] A. Lovato,[1] L. E. Marcucci,[6,7]
Steven C. Pieper,[1] M. Viviani,[6] and R. B. Wiringa[1]
[1]*Physics Division, Argonne National Laboratory, Argonne, Illinois 60439, USA*
[2]*Department of Mathematics and Physics, University of Salento, 73100 Lecce, Italy*
[3]*INFN-Lecce, 73100 Lecce, Italy*
[4]*Theory Center, Jefferson Laboratory, Newport News, Virginia 23606, USA*
[5]*Department of Physics, Old Dominion University, Norfolk, Virginia 23529, USA*
[6]*INFN-Pisa, 56127 Pisa, Italy*
[7]*Department of Physics, University of Pisa, 56127 Pisa, Italy*
(Received 20 June 2016; published 28 November 2016)

We present fully local versions of the minimally nonlocal nucleon-nucleon potentials constructed in a previous paper [Piarulli *et al.*, Phys. Rev. C **91**, 024003 (2015)], and use them in hypersperical harmonics and quantum Monte Carlo calculations of ground and excited states of $^3$H, $^3$He, $^4$He, $^6$He, and $^6$Li nuclei. The long-range part of these local potentials includes one- and two-pion exchange contributions without and with Δ isobars in the intermediate states up to order $Q^3$ ($Q$ denotes generically the low momentum scale) in the chiral expansion, while the short-range part consists of contact interactions up to order $Q^4$. The low-energy constants multiplying these contact interactions are fitted to the 2013 Granada database in two different ranges of laboratory energies, either 0–125 MeV or 0–200 MeV, and to the deuteron binding energy and *nn* singlet scattering length. Fits to these data are performed for three models characterized by long- and short-range cutoffs, $R_L$ and $R_S$, respectively, ranging from $(R_L, R_S) = (1.2, 0.8)$ fm down to $(0.8, 0.6)$ fm. The long-range (short-range) cutoff regularizes the one- and two-pion exchange (contact) part of the potential.

DOI: 10.1103/PhysRevC.94.054007

## I. INTRODUCTION

The understanding of the structure and reactions of nuclei and nuclear matter has been a long-standing goal of nuclear physics. In this respect, few- and many-body systems provide a laboratory for studying nuclear forces with a variety of numerical and computational techniques. In recent years, rapid advances in *ab initio* few- and many-body methods, such as no-core shell model (NCSM) [1,2], coupled cluster (CC) [3,4] and hyperspherical harmonics (HH) [5–8] expansions, similarity renormalization group (SRG) approaches [9,10], self-consistent Green's function techniques [11,12], and quantum Monte Carlo (QMC) methods [13], in combination with the rapid increase in computational resources, have made it possible to test conventional theories and new ones, such as chiral effective field theory (χEFT), in calculations of nuclear structure and reactions.

During the past quarter century, χEFT, originally proposed by Weinberg in the early 1990s [14], has been widely used for the derivation of nuclear forces and electroweak currents. Such a theory provides the most general scheme accommodating all possible interactions among nucleons, Δ isobars, and pions compatible with the relevant symmetries—in particular chiral symmetry—of low-energy quantum chromodynamics (QCD), the underlying theory of strong interactions. By its own nature, χEFT is organized within a given power counting scheme and the resulting chiral potentials (and currents) are systematically expanded in powers of $Q/\Lambda_\chi$ with $Q \ll \Lambda_\chi$, where $Q$ denotes generically a low momentum and $\Lambda_\chi \sim 1$ GeV specifies the chiral-symmetry breaking scale (see Refs. [15,16] for recent review articles).

The power counting of χEFT indicates that nuclear forces are dominated by nucleon-nucleon (*NN*) interactions, a feature which was already known before χEFT was introduced but could be justified more formally with the advent of such a theory [14]. Many-body forces are suppressed by powers of $Q$; however, the inclusion of three-nucleon forces ($3N$) is mandatory at the level of accuracy now reached by few- and many-body calculations (see Refs. [17,18] and references therein for a comprehensive review on this topic). Being the dominant contribution of the nuclear forces, a great deal of attention has been devoted to the derivation and optimization of *NN* interactions.

About a decade ago, *NN* interactions up to next-to-next-to-next-to-leading order (N3LO or $Q^4$) in the chiral expansion were derived [19–28] and quantitative *NN* potentials were developed [29,30] at that order. These N3LO *NN* interactions are separated into pion-exchange contributions and contact terms. Pion-exchange contributions represent the long-range part of the *NN* interactions and include at leading order (LO or $Q^0$) the well-known static one-pion-exchange (OPE) potential and at higher orders, namely next-to-leading (NLO or $Q^2$), next-to-next-to-leading (N2LO or $Q^3$), and N3LO, the two-pion-exchange (TPE) potential due to leading and subleading $\pi N$ couplings. These subleading chiral constants can consistently be obtained from low-energy $\pi N$ scattering data [28,31–33]. Also three-pion exchange ($3\pi$) shows up for the first time at N3LO; in Refs. [21,22], it was demonstrated that the $3\pi$ contributions at this order are negligible. More recently two- and three-pion-exchange contributions that occur at N4LO ($Q^5$) [34,35] and N5LO ($Q^6$) [36] have been investigated.

 

Contact terms encode the short-range physics, and their strength is specified by unknown low-energy constants (LECs). In order to fix these LECs, *NN* chiral potentials have been confronted with the *pp* and *np* scattering databases up to laboratory energy of 300 MeV. These databases have been provided by the Nijmegen group [37,38], the VPI/GWU group [39], and more recently the Granada group [40]. In the standard optimization procedure the potentials are first constrained by fitting *np* and *pp* phase shifts, and then the fit is refined by minimizing the total $\chi^2$ obtained from a direct comparison with the *NN* scattering data. Entem and Machleidt [29] used their N3LO chiral potential to fit *pp* and *np* scattering data in the Nijmegen database up to laboratory energy of 290 MeV with a total $\chi^2$/datum of 1.28. Other available chiral potentials [30] have not been fitted to scattering data directly but rather to phase shifts obtained in the Nijmegen analysis. (The recent upgrade [35] of Ref. [30] relies on this procedure, while in Refs. [34,36] a study of peripheral phase shifts is carried out with two- and three-pion exchange contributions up to order $Q^5$ and $Q^6$, respectively.)

Recently, a different optimization strategy has been introduced by Ekstrom *et al.* [41]. This approach is based on a simultaneous fit of the *NN* and $3N$ forces to low-energy *NN* data, deuteron binding energy, and binding energies and charge radii of hydrogen, helium, carbon, and oxygen isotopes. These authors considered the $NN + 3N$ interaction at N2LO, namely $\mathrm{N2LO_{sat}}$, where the *NN* sector is constrained by *pp* and *np* scattering observables from the SM99 [39] database up to 35 MeV scattering energy in the laboratory system with a total $\chi^2$/datum $\approx 4.3$.

The family of *NN* chiral interactions mentioned above are formulated in momentum space and have the feature of being strongly nonlocal in coordinate space, making them not well suited for certain numerical algorithms, for example, QMC. Up to until recently, QMC methods, such as variational Monte Carlo (VMC), Green's function Monte Carlo (GFMC), and auxiliary field diffusion Monte Carlo (AFDMC), have been used to compute the properties of light nuclei with mass number $A \leqslant 12$, closed-shell nuclei $^{16}$O and $^{40}$Ca, and nucleon matter by using phenomenological nuclear Hamiltonians based on the Argonne $v_{18}$ (AV18) two-nucleon potential [42] and the Urbana/Illinois (U/IL) series of three-nucleon potentials [43–46]. While QMC has had great success in predicting many nuclear properties, such as spectra, electromagnetic form factors, electroweak transitions, low-energy scattering, and response, nevertheless it has been limited to realistic Hamiltonians based on the AV18 and U/IL models and other simpler local interactions. The reason is that local coordinate-space interactions are particularly convenient for QMC techniques, and the AV18 and U/IL models fall into this category, while many of the available *NN* chiral interactions have strong nonlocalities. These nonlocalities come about because of (i) the specific choice made to regularize the momentum space potential and (ii) contact interactions that depend not only on the momentum transfer $\mathbf{k} = \mathbf{p}' - \mathbf{p}$ but also on $\mathbf{K} = (\mathbf{p}' + \mathbf{p})/2$ ($\mathbf{p}$ and $\mathbf{p}'$ are the initial and final relative momenta of the two nucleons).

Local chiral interactions were developed up to N2LO (or $Q^3$) [47,48] only recently. These interactions are regularized in coordinate space by a cutoff depending only on the relative distance between the two nucleons, and use Fierz identities to remove completely the dependence on the relative momentum $-i\,\boldsymbol{\nabla}$ (or equivalently $\mathbf{K}$), by selecting appropriate combinations of contact operators. The LECs multiplying these contact terms have been fixed by performing $\chi^2$ fits to the *np* phase shifts from the Nijmegen partial-wave analysis (PWA) up to 150 MeV laboratory energy. The resulting chiral potentials have been used in GFMC calculations for $A \leqslant 5$ nuclei and AFDMC calculations of neutron matter [48–50]. While this Fierz rearrangement is effective in completely removing nonlocalities at N2LO, it cannot do so at N3LO. As shown in Ref. [51], operator structures depending quadratically on $-i\,\boldsymbol{\nabla}$ are unavoidable, and therefore the potentials constructed in Ref. [51] belong to the class of minimally nonlocal chiral potentials at N(3)LO, where, hereafter, the notation N(3)LO implies that these interactions include the short-range part up to N3LO and the long-range part up to N2LO (see discussion in Sec. II).

In the present work we construct fully local versions of these minimally nonlocal *NN* potentials [51] by dropping the terms proportional to $\boldsymbol{\nabla}^2$, and use them in HH, VMC, and GFMC calculations of ground and excited states of $^3$H, $^3$He, $^4$He, $^6$He, and $^6$Li nuclei. The paper is organized as follows. In the next section we summarize the main points of Ref. [51], and then proceed to discuss the modifications adopted in this work in order to construct the new class of local potentials. In Sec. III we provide the $\chi^2$ values obtained by performing different types of fits to data, show the calculated phase shifts for the lower partial waves (S, P, and D waves), and compare these phase shifts to those from recent PWA's. There we also provide tables of the *pp*, *np*, and *nn* effective range parameters and deuteron properties. In Sec. IV the HH, VMC, and GFMC methods are briefly described and results for the binding energies of $A = 3$, 4, and 6 nuclei are discussed. Clearly, the N(3)LO calculations reported here with only two-body forces are incomplete, since three-body forces start to come in at N2LO. Nevertheless, they provide the basis for the calculations of light nuclei structure based on chiral two- *and* three-body forces (including $\Delta$-isobar degrees of freedom in the intermediate states), which will follow.

## II. LOCAL CHIRAL *NN* POTENTIALS

Following Ref. [51], the local *NN* potential constructed in the present work is written as a sum of an electromagnetic-interaction component, $v_{12}^{\mathrm{EM}}$, and a strong-interaction component, $v_{12}$. The $v_{12}^{\mathrm{EM}}$ interaction is the same as that used in the AV18 potential [42], while the $v_{12}$ one is obtained in $\chi$EFT and is conveniently separated into long- and short-range parts, respectively $v_{12}^{\mathrm{L}}$ and $v_{12}^{\mathrm{S}}$. The $v_{12}^{\mathrm{L}}$ part includes the one-pion-exchange (OPE) and two-pion-exchange (TPE) contributions up to N2LO (or $Q^3$) in the chiral expansion. The TPE component also contains diagrams involving $\Delta$ isobars in intermediate states [51]. It should be noted that strict adherence to power counting would require inclusion of additional one-loop as well as two-loop TPE and three-pion exchange contributions at order $Q^4$. These contributions have been neglected, since they are known to be small (see, for

example, Ref. [16]). Furthermore, it is the LECs at $Q^4$ (denoted as $D_i$ in the tables below) that are critical for a good reproduction of phase shifts in lower partial waves, particularly D waves, and a good fit to the $NN$ database [16] in the 0- to 200-MeV range of energies considered in the present study.

The strength of this long-range part is fully determined by the nucleon and nucleon-to-Δ axial coupling constants $g_A$ and $h_A$, the pion decay amplitude $F_\pi$, and the subleading N2LO LECs $c_1$, $c_2$, $c_3$, $c_4$, and $b_3 + b_8$, constrained by reproducing $\pi N$ scattering data [28]. Note that the LEC $(b_3 + b_8)$ is explicitly retained in our fitting procedure, even though it has been shown to be redundant at this order [52]. Here and in what follows, we adopt the same values for pion and nucleon masses, $F_\pi$, $g_A$, and $h_A$ and the subleading N2LO LECs as listed in Tables I and II of Ref. [51].

The potential $v_{12}^{\rm L}$ can be written in coordinate space as a sum of eight operators,

$$v_{12}^{\rm L} = \left[\sum_{l=1}^{6} v_{\rm L}^{l}(r)\, O_{12}^{l}\right] + v_{\rm L}^{\sigma T}(r)\, O_{12}^{\sigma T} + v_{\rm L}^{tT}(r)\, O_{12}^{tT}, \quad (1)$$

where

$$O_{12}^{l=1,\ldots,6} = [\mathbf{1}\,, \boldsymbol{\sigma}_1\cdot\boldsymbol{\sigma}_2\,, S_{12}] \otimes [\mathbf{1}\,, \boldsymbol{\tau}_1\cdot\boldsymbol{\tau}_2], \quad (2)$$

$O_{12}^{\sigma T} = \boldsymbol{\sigma}_1\cdot\boldsymbol{\sigma}_2\, T_{12}$, and $O_{12}^{tT} = S_{12}\, T_{12}$, and $T_{12} = 3\,\tau_{1z}\tau_{2z} - \boldsymbol{\tau}_1\cdot\boldsymbol{\tau}_2$ is the isotensor operator. The first six terms (the so-called $v_6$ operator structure) in Eq. (1) are the charge-independent (CI) central, spin, and tensor components without and with the isospin dependence $\boldsymbol{\tau}_1\cdot\boldsymbol{\tau}_2$, while the last two terms (proportional to $T_{12}$) are the charge-independence breaking (CIB) central and tensor components induced by the difference between the neutral and charged pion masses in the OPE. The radial functions $v_{\rm L}^{l}(r)$, $v_{\rm L}^{\sigma T}(r)$, and $v_{\rm L}^{tT}(r)$ are explicitly given in Appendix A of Ref. [51]. The singularities at the origin are regularized by cutoff functions of the form

$$C_{R_{\rm L}}(r) = 1 - \frac{1}{(r/R_{\rm L})^6\, e^{(r-R_{\rm L})/a_{\rm L}} + 1}, \quad (3)$$

where three values for the radius $R_{\rm L}$ are considered, $R_{\rm L} = (0.8, 1.0, 1.2)$ fm with the diffuseness $a_{\rm L}$ fixed at $a_{\rm L} = R_{\rm L}/2$ in each case.

The main difference between the potentials constructed in Ref. [51] and those in the current work lies in the operator structure of their short-range components, which we now take to have the form

$$v_{12}^{\rm S} = \sum_{l=1}^{16} v_{\rm S}^{l}(r)\, O_{12}^{l}, \quad (4)$$

where $O_{12}^{l=1,\ldots,6}$ have been defined above,

$$O_{12}^{l=7,\ldots,11} = \mathbf{L}\cdot\mathbf{S}\,, \mathbf{L}\cdot\mathbf{S}\,\boldsymbol{\tau}_1\cdot\boldsymbol{\tau}_2\,, (\mathbf{L}\cdot\mathbf{S})^2\,, \mathbf{L}^2\,, \mathbf{L}^2\,\boldsymbol{\sigma}_1\cdot\boldsymbol{\sigma}_2\,, \quad (5)$$

and

$$O_{12}^{l=12,\ldots,16} = T_{12}\,, \left(\tau_1^z + \tau_2^z\right), \boldsymbol{\sigma}_1\cdot\boldsymbol{\sigma}_2\, T_{12}, S_{12}\, T_{12}\,, \mathbf{L}\cdot\mathbf{S}\, T_{12}. \quad (6)$$

The parametrization above differs in two ways from that of the minimally nonlocal potential of Ref. [51]. The first difference concerns the $\mathbf{p}^2$ terms

$$\left\{ v_{\rm S}^{p}(r) + v_{\rm S}^{p\sigma}(r)\,\boldsymbol{\sigma}_1\cdot\boldsymbol{\sigma}_2 + v_{\rm S}^{pt}(r)\, S_{12} + v_{\rm S}^{pt\tau}(r)\, S_{12}\,\boldsymbol{\tau}_1\cdot\boldsymbol{\tau}_2\ ,\ \mathbf{p}^2 \right\},$$

which are now absent in Eq. (4); i.e., the LECs mutliplying these contact terms are enforced to vanish in the fits to follow. The second difference has to do with the charge-symmetry breaking (CSB) piece of $v_{12}^{\rm S}$, which, in contrast to Ref. [51], includes only the LO term proportional to $(\tau_1^z + \tau_2^z)$ needed to reproduce the singlet $nn$ scattering length.

The radial functions $v_{\rm S}^{l}(r)$ are the same as those listed in Appendix B of Ref. [51] and involve a local regulator (to replace the $\delta$ functions) taken as

$$C_{R_{\rm S}}(r) = \frac{1}{\pi^{3/2} R_{\rm S}^3}\, e^{-(r/R_{\rm S})^2}, \quad (7)$$

where we consider, in combination with $R_{\rm L} = (0.8, 1.0, 1.2)$ fm, $R_{\rm S} = (0.6, 0.7, 0.8)$ fm, corresponding to typical momentum-space cutoffs $\Lambda_{\rm S} = 2/R_{\rm S}$ ranging from about 660 MeV down to 500 MeV. Hereafter we will denote the potential with cutoffs $(R_{\rm L}, R_{\rm S}) = (1.2, 0.8)$ fm as model $a$, that with (1.0,0.7) fm as model $b$, and that with (0.8,0.6) fm as model $c$. These radial functions contain 26 LECs. Of these, 20 are in the charge-independent part of $v_{12}^{\rm S}$: 2 at LO ($Q^0$), 7 at NLO ($Q^2$), and 11 at N(3)LO ($Q^4$). The remaining 6 are in its charge-dependent part: 2 at LO (one each from CIB and CSB), and 4 at NLO from CIB. The optimization procedure to fix these 26 LECs is the same as that adopted in Ref. [51] and is discussed in the next section. It uses $pp$ and $np$ scattering data (including normalizations), as assembled in the Granada database [40], the $nn$ scattering length, and the deuteron binding energy. The minimization of the objective function $\chi^2$ with respect to the LECs is carried out with the Practical Optimization Using No Derivatives (for Squares), POUNDerS [53].

## III. TOTAL $\chi^2$ AND PHASE SHIFTS

We report results for the local potentials $v_{12} + v_{12}^{\rm EM}$ described in the previous section and corresponding to three different choices of cutoffs $(R_{\rm L}, R_{\rm S})$: model $a$ with (1.2,0.8) fm, model $b$ with (1.0,0.7) fm, and model $c$ with (0.8,0.6) fm. Models $a$, $b$, and $c$ are fitted to the Granada database of $pp$ and $np$ observables in two different ranges of laboratory energies, either 0–125 or 0–200 MeV, to the deuteron binding energy and $nn$ singlet scattering length. For convenience potential models $a$, $b$, and $c$ fitted up to 200-MeV laboratory energy are labeled as $\widetilde{a}$, $\widetilde{b}$ and $\widetilde{c}$, respectively. We list the total number of $pp$ and $np$ data (including normalizations) and corresponding total $\chi^2$ per datum for all the potentials in Table I. The total number of data points, $N_{pp+np}$, changes slightly for each of the various models because of fluctuations in the number of normalizations (see Ref. [51] for more details on the fit procedure). For model $b$ we performed fits of the Granada database up to 125 MeV order by order in the chiral expansion. The total $\chi^2$/datum are 59.88, 2.18, 2.32, and 1.07 at LO, NLO, N2LO, and N(3)LO, respectively. There is a strong reduction in the total $\chi^2$ going from LO and NLO and from N2LO and N(3)LO. However,

TABLE I. Total $\chi^2$/datum for model $a$ ($\tilde{a}$) with $(R_L, R_S) =$ (1.2,0.8) fm, model $b$ ($\tilde{b}$) with (1.0,0.7) fm, and model $c$ ($\tilde{c}$) with (0.8,0.6) fm fitted up to 125 (200) MeV laboratory energy. For model $b$, results of the fits up to 125 MeV order by order in the chiral expansion are also given; $N_{pp+np}$ denotes the total number of $pp$ and $np$ data, including observables and normalizations. The last three rows list the $\chi^2$/datum obtained (*without refitting*) with models $a$, $b$, and $c$ over the energy range 0–200 MeV.

| Model | Order | $E_{\rm Lab}$ (MeV) | $N_{pp+np}$ | $\chi^2$/datum |
|---|---|---|---|---|
| $b$ | LO | 0–125 | 2558 | 59.88 |
| $b$ | NLO | 0–125 | 2648 | 2.18 |
| $b$ | N2LO | 0–125 | 2641 | 2.32 |
| $b$ | N(3)LO | 0–125 | 2665 | 1.07 |
| $a$ | N(3)LO | 0–125 | 2668 | 1.05 |
| $c$ | N(3)LO | 0–125 | 2666 | 1.11 |
| $\tilde{a}$ | N(3)LO | 0–200 | 3698 | 1.37 |
| $\tilde{b}$ | N(3)LO | 0–200 | 3695 | 1.37 |
| $\tilde{c}$ | N(3)LO | 0–200 | 3693 | 1.40 |
| $a$ | N(3)LO | 0–200 | 3690 | 2.41 |
| $b$ | N(3)LO | 0–200 | 3679 | 3.76 |
| $c$ | N(3)LO | 0–200 | 3679 | 4.52 |

the quality of the fit worsens slightly in going from NLO to N2LO. At N2LO we fixed the chiral LECs, namely $c_1$, $c_2$, $c_3$, $c_4$, and $b_3 + b_8$, from the $\pi N$ scattering analysis of Ref. [28]. In the range 0- to 125-MeV, the total $\chi^2$/datum at N(3)LO are 1.05, 1.07, and 1.11 for models $a$, $b$, and $c$, respectively; while in the range 0- to 200-MeV the total $\chi^2$/datum at N(3)LO are 1.37, 1.37, and 1.40. The total $\chi^2$/datum at N(3)LO for models $a$, $b$, and $c$ when compared (without refitting) to the 0- to 200-MeV database are 2.41, 3.76, and 4.52, respectively. In both energy ranges, the quality of the fits deteriorates slightly as the $(R_L, R_S)$ cutoffs are reduced from the values (1.2,0.8) fm of model $a$ down to (0.8,0.6) fm of model $c$.

The fitted values of the LECs corresponding to models $a$, $b$, $c$ and $\tilde{a}$, $\tilde{b}$, $\tilde{c}$ are listed in Tables II and III, respectively. The values for the $\pi N$ LECs in the OPE and TPE terms of these models are given in Table I of Ref. [51].

The $np$ and $pp$ S-wave, P-wave, and D-wave phase shifts for potential models fitted up to 125 and 200 MeV laboratory energy are displayed in Figs. 1 and 2, respectively. The top two panels of these figures show the phase shifts for $np$ in $T = 1$ and $T = 0$ channels, respectively, while the remaining bottom panels show the $pp$ phase shifts (in $T = 1$ channel). The width of the shaded band represents the cutoff sensitivity of the phases obtained with the full models $a$, $b$, and $c$, including strong and electromagnetic interactions. The calculated phases are compared to those obtained in PWA's by the Nijmegen [37], Granada [40], and Gross-Stadler [54] groups. The recent Gross-Stadler PWA is limited to $np$ data only.

In Fig. 3, the $np$ (top panels) and $pp$ (lower panel) S-wave, P-wave, and D-wave phase shifts are displayed for model $b$ up to 125 MeV laboratory energy order by order in the chiral expansion. Dashed (blue), dash-dotted (green), double-dash-dotted (magenta), and solid (red) lines represent the results at LO, NLO, N2LO, and N(3)LO, respectively.

TABLE II. Values of the LECs corresponding to potential models $a$, $b$, and $c$ (fitted up to 125 MeV laboratory energy). The notation $(\pm n)$ means $\times 10^{\pm n}$.

| LECs | Model $a$ | Model $b$ | Model $c$ |
|---|---|---|---|
| $C_S$ (fm$^2$) | 0.2726141(+1) | 0.8038124(+1) | 0.1858356(+2) |
| $C_T$ (fm$^2$) | −0.5228448 | −0.1203741(+1) | −0.6118406(+1) |
| $C_1$ (fm$^4$) | −0.6992838(−1) | −0.2280422 | −0.5624246 |
| $C_2$ (fm$^4$) | −0.1496013 | −0.2249889 | −0.3529711 |
| $C_3$ (fm$^4$) | −0.2502401(−1) | −0.4007665(−1) | −0.2225345 |
| $C_4$ (fm$^4$) | −0.2728396(−1) | 0.1243960(−1) | 0.3381613(−1) |
| $C_5$ (fm$^4$) | −0.6530008(−2) | −0.1870727(−1) | −0.2881762(−1) |
| $C_6$ (fm$^4$) | −0.7554924(−1) | −0.7406609(−1) | −0.6535759(−1) |
| $C_7$ (fm$^4$) | −0.1017206(+1) | −0.1197452(+1) | −0.1464748(+1) |
| $D_1$ (fm$^6$) | −0.4251199(−1) | −0.3820959(−1) | −0.2163208(−1) |
| $D_2$ (fm$^6$) | −0.5567938(−2) | −0.5343034(−2) | 0.2866318(−2) |
| $D_3$ (fm$^6$) | −0.1666607(−1) | −0.1601394(−1) | −0.1472287(−1) |
| $D_4$ (fm$^6$) | 0.1054347(−2) | 0.4219347(−2) | 0.1052796(−2) |
| $D_5$ (fm$^6$) | 0.5383828(−2) | 0.8971752(−2) | 0.7477159(−2) |
| $D_6$ (fm$^6$) | −0.8012050(−2) | −0.5986245(−2) | −0.2247046(−2) |
| $D_7$ (fm$^6$) | −0.2309392(−1) | −0.6180197(−2) | 0.3616700(−1) |
| $D_8$ (fm$^6$) | 0.1383136(−1) | 0.1782567(−1) | 0.2903320(−1) |
| $D_9$ (fm$^6$) | 0.4797012(−1) | 0.3094851(−1) | 0.9175910(-1) |
| $D_{10}$ (fm$^6$) | −0.1156876 | −0.8073891(−1) | −0.1229688 |
| $D_{11}$ (fm$^6$) | −0.1453295(−1) | −0.1162060(−1) | −0.2671576(−1) |
| $C_0^{\rm IV}$ (fm$^2$) | 0.9325477(−2) | 0.1018989(−1) | 0.1357818(−1) |
| $C_0^{\rm IT}$ (fm$^2$) | 0.1578240(−1) | 0.2416591(−1) | 0.2195881(−1) |
| $C_1^{\rm IT}$ (fm$^4$) | −0.2179452(−2) | −0.3707396(−2) | −0.2698274(−2) |
| $C_2^{\rm IT}$ (fm$^4$) | −0.6288540(−2) | −0.3601899(−2) | −0.1288174(−2) |
| $C_3^{\rm IT}$ (fm$^4$) | −0.5799803(−2) | −0.4559006(−2) | −0.3126089(−3) |
| $C_4^{\rm IT}$ (fm$^4$) | 0.2250167(−1) | 0.1859997(−1) | 0.8987538(−2) |

Of course, the description of the phase shifts improves substantially, as one progresses from LO to N(3)LO. The low-energy scattering parameters are listed in Table IV, where they are compared to experimental results [55–59]. The singlet and triplet $np$, and singlet $pp$ and $nn$, scattering lengths are calculated with the inclusion of electromagnetic interactions. Without the latter, the effective range function is simply given by $F(k^2) = k \cot\delta = -1/a + r\,k^2/2$ up to terms linear in $k^2$. In the presence of electromagnetic interactions, a more complicated effective range function must be used; it is reported in Appendix D of Ref. [51], along with the relevant references.

The static deuteron properties are shown in Table V and compared to experimental values [60–63]. The binding energy $E_d$ is fitted exactly and includes the contributions (about 20 keV) of electromagnetic interactions, among which the largest is that due to the magnetic moment term. The asymptotic S-state normalization, $A_S$, deviates less than 1% from the experimental data, and the D/S ratio, $\eta$, is ∼2 standard deviations from experiment for all models considered. The deuteron (matter) radius, $r_d$, is underpredicted by about 0.2–1.0%. It should be noted that this observable has negligible contributions due to two-body electromagnetic operators [64]. The magnetic moment, $\mu_d$, and quadrupole moment, $Q_d$, experimental values are underestimated by all models, but

TABLE III. Same as Table II but for potential models $\widetilde{a}$, $\widetilde{b}$, and $\widetilde{c}$ (fitted up to 200 MeV laboratory energy).

| LECs | Model $\widetilde{a}$ | Model $\widetilde{b}$ | Model $\widetilde{c}$ |
|---|---|---|---|
| $C_S$ (fm$^2$) | 0.2936041(+1) | 0.8398499(+1) | 0.1858331(+2) |
| $C_T$ (fm$^2$) | −0.4933897 | −0.1207696(+1) | −0.6116424(+1) |
| $C_1$ (fm$^4$) | −0.1013462 | −0.2324413 | −0.5565484 |
| $C_2$ (fm$^4$) | −0.1444844 | −0.2108143 | −0.3574422 |
| $C_3$ (fm$^4$) | −0.3647634(−1) | −0.3461629(−1) | −0.2266117 |
| $C_4$ (fm$^4$) | −0.1630825(−1) | 0.8748772(−2) | 0.3921168(−1) |
| $C_5$ (fm$^4$) | −0.6658100(−2) | −0.3614304(−1) | −0.2661419(−1) |
| $C_6$ (fm$^4$) | −0.6176835(−1) | −0.5542581(−1) | −0.6532432(−1) |
| $C_7$ (fm$^4$) | −0.9578191 | −0.1019849(+1) | −0.1465875(+1) |
| $D_1$ (fm$^6$) | −0.3102824(−1) | −0.1193597(−1) | −0.2144023(−1) |
| $D_2$ (fm$^6$) | −0.4438695(−2) | −0.4450346(−2) | 0.1386494(−2) |
| $D_3$ (fm$^6$) | −0.1351171(−1) | −0.9542801(−2) | −0.1620926(−1) |
| $D_4$ (fm$^6$) | −0.7084459(−3) | 0.3976205(−2) | 0.2071219(−2) |
| $D_5$ (fm$^6$) | 0.1110108(−1) | 0.7809205(−2) | 0.7238077(−2) |
| $D_6$ (fm$^6$) | −0.8598857(−2) | −0.7362895(−2) | −0.2323562(−2) |
| $D_7$ (fm$^6$) | −0.5367908(−1) | −0.4158494(−2) | 0.3065351(−1) |
| $D_8$ (fm$^6$) | 0.3119241(−1) | 0.1090986(−1) | 0.2957488(−1) |
| $D_9$ (fm$^6$) | 0.3281636(−1) | 0.6095858(−3) | 0.9135194(−1) |
| $D_{10}$ (fm$^6$) | −0.8647128(−1) | −0.5432144(−1) | −0.1196465 |
| $D_{11}$ (fm$^6$) | −0.1167788(−1) | −0.5186422(−2) | −0.3065569(−1) |
| $C_0^{\rm IV}$ (fm$^2$) | 0.9575695(−2) | 0.1077541(−1) | 0.1312712(−1) |
| $C_0^{\rm IT}$ (fm$^2$) | 0.2194758(−1) | 0.2102140(−1) | 0.1394723(−1) |
| $C_1^{\rm IT}$ (fm$^4$) | −0.1550501(−2) | 0.1152693(−3) | −0.8965197(−2) |
| $C_2^{\rm IT}$ (fm$^4$) | −0.8354679(−2) | −0.1391786(−2) | −0.3079018(−2) |
| $C_3^{\rm IT}$ (fm$^4$) | −0.6682746(−2) | −0.3194459(−3) | 0.3905867(−4) |
| $C_4^{\rm IT}$ (fm$^4$) | 0.1276971(−1) | 0.2879873(−2) | 0.8844043(−3) |

these observables are known to have significant corrections from (isoscalar) two-body terms in nuclear electromagnetic charge and current operators [64]. Their inclusion would bring the calculated values considerably closer to experiment.

Finally, we observe that inclusion of the $\mathbf{p}^2$-dependent terms would have improved only marginally the fits to the database in the energy range 0–200 MeV. For example, in the case of the $\widetilde{b}$ model the value of the $\chi^2$/datum would have been reduced from the current 1.37 to 1.34. The present fits in the range 0–125 MeV already have $\chi^2$/datum close to 1 (in fact less than 1.1 for models $a$ and $b$) and are therefore to be considered statistically satisfactory. However, apart from the small improvement that the $\mathbf{p}^2$-dependent terms would bring to the total $\chi^2$ in the fit to the $NN$ scattering data, the effect of these terms on nuclear observables has not been studied.

## IV. HH AND QMC CALCULATIONS FOR LIGHT NUCLEI

The study of light nuclei is especially interesting since it provides the opportunity to test, in essentially exact numerical calculations, models of two- and three-nucleon forces. In this section, we briefly discuss the HH and QMC methods adopted here for the accurate or exact solution of the few-nucleon Schrödinger equation, $H\,\Psi = E\,\Psi$, where $\Psi$ is a nuclear wave function with specific spin, parity, and isospin. We then present results for the binding energies and rms radii of the $A = 2$–

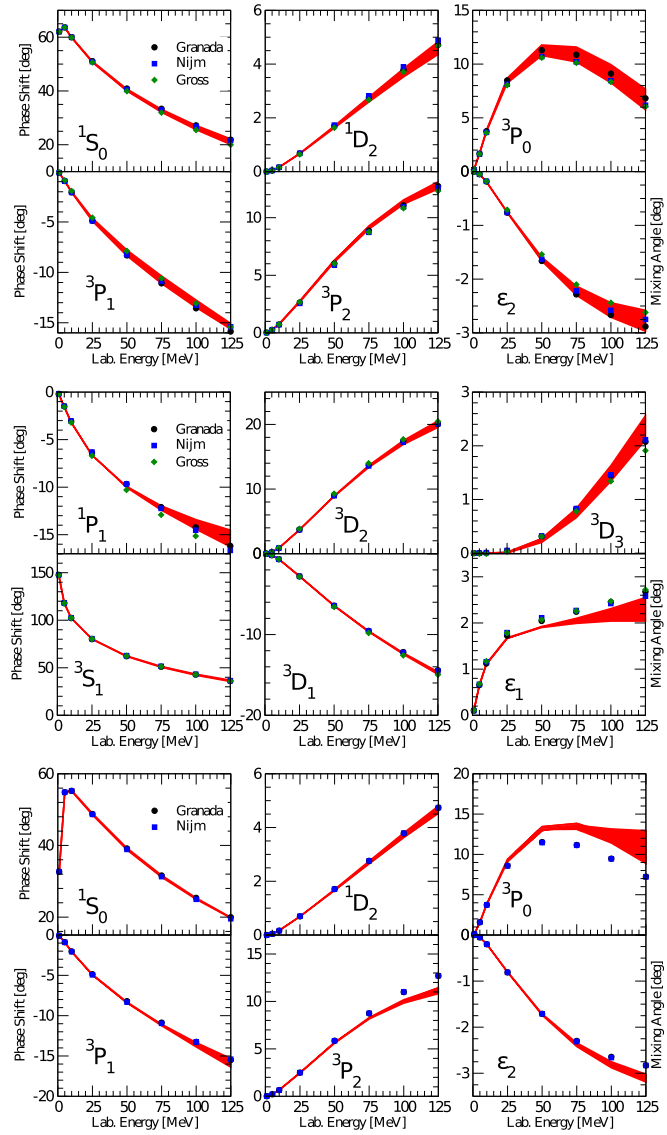


FIG. 1. S-wave, P-wave, and D-wave phase shifts for $np$ in $T = 0$ and 1 states (top two panels) and $pp$ (lower panel), obtained in the Nijmegen [37,38], Gross and Stadler [54], and Granada [40] PWA's, are compared to those of models $a$, $b$, and $c$, indicated by the band.

6 nuclei with a Hamiltonian $H$ including the nonrelativistic kinetic energy in combination with the two-body potentials $v_{12}$ of Sec. II. In particular for our calculations we use nuclear wave functions corresponding to models $a$, $\widetilde{a}$ and $b$, $\widetilde{b}$, whose LECs are specified in Tables II and III.

The HH method is used to calculate the ground-state energies of $^3$H and $^4$He and these results provide a benchmark for the corresponding QMC calculations. The QMC methods are then applied to compute binding energies and rms radii of the $^3$He ground state and of the $^6$Li and $^6$He ground and excited states.

### A. The hyperspherical harmonics method

The HH method uses hyperspherical harmonics functions as a suitable expansion basis for the wave function of an

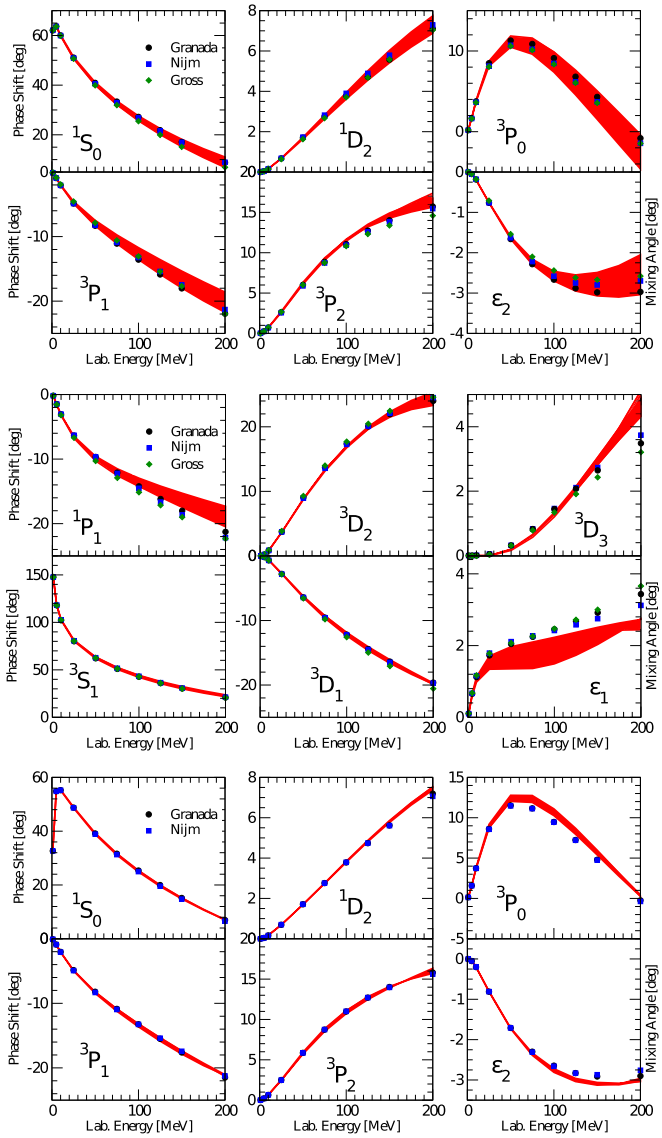


FIG. 2. Same as Fig. 1 but for models $\widetilde{a}$, $\widetilde{b}$, and $\widetilde{c}$ fitted to 200 MeV laboratory energy.

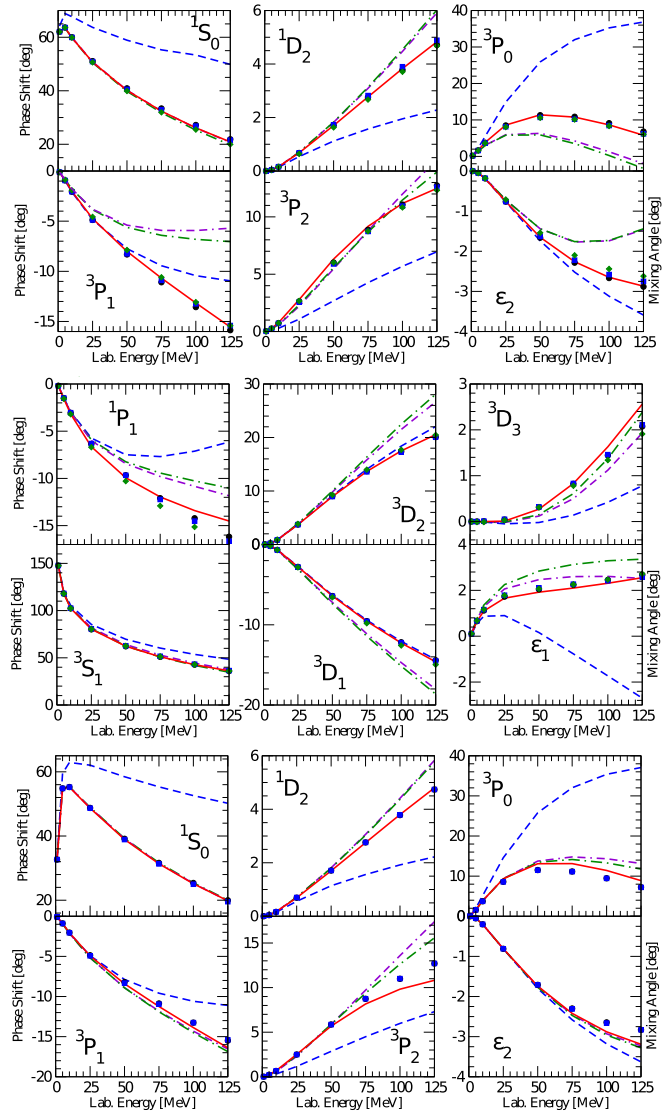


FIG. 3. Chiral expansion of the *np* (top two panels) and *pp* (bottom panel) S-wave, P-wave, and D-wave phase shifts up to 125 MeV for model *b* in comparison with the Nijmegen [37,38], Gross and Stadler [54], and Granada [40] PWA's. Dashed (blue), dash-dotted (green), double-dash-dotted (magenta), and solid (red) lines show the results at LO, NLO, N2LO and N(3)LO, respectively.

$A$-body system. In the specific case of $A=3$ and 4 nuclei, the corresponding ground-state wave functions $\Psi_A^{J^\pi}$ ($J^\pi$ being the total angular momentum and parity) can be expanded in the following way:

$$\Psi_3^{1/2^+} = \sum_{[K_3]} u_{[K_3]}(\rho_3)\mathcal{B}_{[K_3]}(\Omega_3) \tag{8}$$

and

$$\Psi_4^{0^+} = \sum_{[K_4]} u_{[K_4]}(\rho_4)\mathcal{B}_{[K_4]}(\Omega_4)\,. \tag{9}$$

Here $\mathcal{B}_{[K_3]}(\Omega_3)$ and $\mathcal{B}_{[K_4]}(\Omega_4)$ are fully antisymmetrized HH-spin-isospin functions for three and four nucleons characterized by the set of quantum numbers $[K_3] \equiv [n_1,l_1,l_2,L,s,S,t,T]$ and $[K_4] \equiv [n_1,n_2,l_1,l_2,l_3,l',L,s,s',S,t,t',T]$ respectively. The quantum numbers $n_i,l_i$ and $l'$ enter in the construction of the HH vector and are such that the grand angular momenta are $K_3 = 2n_1 + l_1 + l_2$ and $K_4 = 2n_1 + 2n_2 + l_1 + l_2 + l_3$. The orbital angular momenta $l_i$ (and $l'$ for $A=4$) are coupled to give the total orbital angular momentum $L$. The total spin and isospin of the vector are indicated with $S$ and $T$, respectively, and $s,s',t,t'$ are intermediate couplings. A detailed description of the HH method with the explicit expression of the HH-spin-isospin functions can be found in Refs. [65–68].

The hyperspherical coordinates $(\rho_A,\Omega_A)$ in Eqs. (8) and (9) are given by the hyper-radius, $\rho_A^2 = \sum_{i=1}^{A-1} \mathbf{x}_i^2$ expressed in terms of the $A$–1 Jacobi vectors $\mathbf{x}_i$ of the systems, and the hyperangles $\Omega_A = (\hat{\mathbf{x}}_1 \ldots \hat{\mathbf{x}}_{A-1}, \alpha_2 \ldots \alpha_{A-1})$, with $\hat{\mathbf{x}}_i$ being the unit Jacobi vectors and $\alpha_i$ the hyperangular variables. For

TABLE IV. The singlet and triplet $np$, and singlet $pp$ and $nn$, scattering lengths and effective ranges corresponding to the potential models $a$, $b$, and $c$ (fitted up to 125 MeV laboratory energy), and $\widetilde{a}$, $\widetilde{b}$, and $\widetilde{c}$ (fitted up to 200 MeV laboratory energy). Experimental values are from Refs. [55–59].

| | Experiment | Model $a$ | Model $b$ | Model $c$ | Model $\widetilde{a}$ | Model $\widetilde{b}$ | Model $\widetilde{c}$ |
|---|---|---|---|---|---|---|---|
| $^1a_{pp}$ | −7.8063(26)<br>−7.8016(29) | −7.776 | −7.774 | −7.769 | −7.775 | −7.770 | −7.769 |
| $^1r_{pp}$ | 2.794(14)<br>2.773(14) | 2.780 | 2.771 | 2.754 | 2.774 | 2.760 | 2.753 |
| $^1a_{nn}$ | −18.90(40) | −18.896 | −18.921 | −18.966 | −18.904 | −19.009 | −18.919 |
| $^1r_{nn}$ | 2.75(11) | 2.825 | 2.815 | 2.795 | 2.819 | 2.801 | 2.794 |
| $^1a_{np}$ | −23.740(20) | −23.722 | −23.739 | −23.741 | −23.758 | −23.754 | −23.740 |
| $^1r_{np}$ | 2.77(5) | 2.666 | 2.686 | 2.684 | 2.642 | 2.682 | 2.683 |
| $^3a_{np}$ | 5.419(7) | 5.424 | 5.424 | 5.423 | 5.399 | 5.394 | 5.424 |
| $^3r_{np}$ | 1.753(8) | 1.761 | 1.760 | 1.770 | 1.727 | 1.720 | 1.773 |

$A = 3, \cos\alpha_2 = x_2/\rho_3$, and for $A = 4, \cos\alpha_2 = x_2/\sqrt{x_1^2 + x_2^2}$ and $\cos\alpha_3 = x_3/\rho_4$ [68].

In the present application of the HH method, the hyper-radial functions are in turn expanded in terms of generalized Laguerre polynomials multiplied by an exponential function

$$u_\mu(\rho_A) = \sum_m C_{m,\mu}\ \mathcal{L}_m^{(3A-4)}(z)\ e^{-z/2}\ , \tag{10}$$

with $z = \beta\rho_A$, $\beta$ being a nonlinear parameter, and $\mu \equiv [K_A]$. Introducing the above expansion in Eqs. (8) and (9), we can rewrite $\Psi_A^{J^\pi}$ in the compact form

$$\Psi_A^{J^\pi} = \sum_{m,\mu} C_{m,\mu}\ \Phi_{m,\mu}(\rho_A, \Omega_A)\ , \tag{11}$$

where the (normalized) complete antisymmetric vectors are

$$\Phi_{m,\mu}(\rho_A, \Omega_A) = \mathcal{L}_m^{(3A-4)}(z) e^{-z/2} \mathcal{B}_{[K_A]}(\Omega_A). \tag{12}$$

The ground-state energy $E$ is obtained by applying the Rayleigh-Ritz variational principle, which leads to the following eigenvalue-eigenstate problem:

$$\sum_{m',\mu'} (H_{m\mu,m'\mu'} - E\, I_{m\mu,m'\mu'}) = 0, \tag{13}$$

where $H_{m\mu,m'\mu'}$ are the Hamiltonian matrix elements $\langle m\mu|H|m'\mu'\rangle$ and $I_{m\mu,m'\mu'}$ indicates the matrix elements of the identity matrix. The convergence of the energy $E$ in terms of the size of the basis is studied as follows. The HH functions are collected in channels having specific combinations of the HH-spin-isospin quantum numbers. For the three-nucleon system the basis includes all possible combinations of HH functions up to $l_1 + l_2 = 6$ corresponding to 23 angular-spin-isospin channels with isospin components $T = 1/2, 3/2$. For each channel the hyperangular quantum number $n_1$ and hyper-radial quantum number $m$ are increased until convergence is reached at a level of accuracy of the order of a few keV on the sought energy eigenvalue. In the case of $A = 4$ all possible combinations of HH functions up to $l_1 + l_2 + l_3 = 6$ having $T = 0$ are included, while for the wave function components having $T > 0$ HH-spin-isospin states up to $l_1 + l_2 + l_3 = 2$ are considered. This selection corresponds to about 234 angular-spin-isospin channels. For each channel the hyperangular quantum numbers $n_1, n_2$ and hyper-radial quantum number $m$ are increased until convergence is reached at a satisfactory level of accuracy. Detailed studies of the convergence have been done in Ref. [67], showing that with this kind of expansion an accuracy of about 20 keV can be obtained for the $^4$He ground-state energy.

### B. Quantum Monte Carlo methods

Over the past three decades, QMC methods have been successfully used to study the structure and reactions of light nuclei and nucleonic matter starting from phenomenological interactions. The extensive use of these *ab initio* methods for computing many of the important properties of light nuclei, such as spectra, form factors, radiative and weak transitions, low-energy scattering, and electroweak response, has led to a rather large number of references, where detailed descriptions of QMC algorithms, as well as tests of their accuracy, have been described in detail and discussed at length (see, for example,

TABLE V. Same as in Table IV but for the deuteron static properties; experimental values are from Refs. [60–63].

| | Experiment | Model $a$ | Model $b$ | Model $c$ | Model $\widetilde{a}$ | Model $\widetilde{b}$ | Model $\widetilde{c}$ |
|---|---|---|---|---|---|---|---|
| $E_d$ (MeV) | 2.224575(9) | 2.224574 | 2.224573 | 2.224576 | 2.224574 | 2.224568 | 2.224570 |
| $A_S$(fm$^{-1/2}$) | 0.8846(9) | 0.8862 | 0.8861 | 0.8874 | 0.8811 | 0.8799 | 0.8877 |
| $\eta$ | 0.0256(4) | 0.0249 | 0.0248 | 0.0250 | 0.0247 | 0.0245 | 0.0250 |
| $r_d$ (fm) | 1.97535(85) | 1.968 | 1.968 | 1.971 | 1.956 | 1.955 | 1.971 |
| $\mu_d$ ($\mu_0$) | 0.857406(1) | 0.850 | 0.849 | 0.850 | 0.850 | 0.850 | 0.849 |
| $Q_d$ (fm$^2$) | 0.2859(3) | 0.268 | 0.267 | 0.269 | 0.263 | 0.256 | 0.269 |
| $P_d$(%) | | 5.24 | 5.49 | 5.32 | 5.22 | 5.21 | 5.35 |

the review article [13] and references therein for a complete overview of the topic). In this section we briefly outline those features of QMC techniques relevant for the implementation of these methods with the present chiral (and local) *NN* potentials at N(3)LO.

The QMC calculations proceed in two steps. The first step is the variational Monte Carlo (VMC) calculation, in which trial wave functions are optimized by minimizing the Hamiltonian. The second consists of the Green's function Monte Carlo (GFMC) calculation, in which the exact wave functions of the nuclear Hamiltonian are projected out of these optimized trial wave functions by evolving them in imaginary time.

In VMC calculations, one assumes a suitably parametrized form for the antisymmetric wave function $\Psi_T$ of a given spin, parity, and isospin and optimizes the variational parameters by minimizing the energy expectation value, $E_T$,

$$E_T = \frac{\langle \Psi_T | H | \Psi_T \rangle}{\langle \Psi_T | \Psi_T \rangle} \geqslant E_0, \tag{14}$$

which is evaluated by Metropolis Monte Carlo integration [69]. The lowest value for $E_T$ is then taken as the approximate ground-state energy. Upper bounds to energies of excited states can also be obtained, either from standard VMC calculations if they have different quantum numbers from the ground state, or from small-basis diagonalizations if they have the same quantum numbers.

The best variational wave functions $\Psi_T$ for the nuclei studied in the present work have the form [70]

$$|\Psi_T\rangle = S \prod_{i<j}^{A} (1 + U_{ij}) \, |\Psi_J\rangle, \tag{15}$$

where $S$ is the symmetrization operator. The Jastrow wave function $\Psi_J$ is fully antisymmetric and has the $(J^\pi; T)$ quantum numbers of the state of interest, while $U_{ij}$ are the two-body correlation operators. The correlation functions in $U_{ij}$ are obtained by solving two-body Euler-Lagrange equations projected in pair spin $S$ and isospin $T$ channels, and for finite nuclei are required to satisfy suitable boundary conditions [70]. Since the calculations carried out here are with only two-body interactions, three-body correlations induced by three-body interactions are not explicitly accounted for in $\Psi_T$.

In order to find the optimum $\Psi_T$, the minimization of the energy expectation value and its associated variance are carried out with respect to the variational parameters. In the case of $A = 6$ nuclei, the optimization of the energies is subject to the constraint that the rms radii are close to the GFMC ones obtained with the AV18. This is because the best variational wave functions we have do not make $p$-shell nuclei stable against breakup into subclusters.

Given the best set of variational parameters, the trial wave function $\Psi_T$ can then be used as the starting point of a GFMC [71,72] calculation which projects out of it the exact lowest energy state $\Psi_0$ with the same quantum numbers. The projection of $\Psi_0$ is carried out by evolving for long imaginary time $\tau = -i\,t$

$$|\Psi_0\rangle \propto \lim_{\tau\to\infty} |\Psi(\tau)\rangle = \lim_{\tau\to\infty} e^{-(H-E_0)\,\tau} \, |\Psi_T\rangle, \tag{16}$$

with the obvious initial condition $|\Psi(\tau{=}0)\rangle = |\Psi_T\rangle$. In practice the imaginary-time evolution operator $\exp[-(H - E_0)\,\tau]$ is computed for small time steps $\Delta\tau$ with $\tau = n\,\Delta\tau$, and is carried out with a simplified version $H'$ of the full Hamiltonian $H$. In the presence of only *NN* interactions the Hamiltonian $H'$ contains a charge-independent eight-operator projection, $[\mathbf{1}\,, \boldsymbol{\sigma}_1 \cdot \boldsymbol{\sigma}_2\,, S_{12}\,, \mathbf{L}\cdot\mathbf{S}] \otimes [\mathbf{1}\,, \boldsymbol{\tau}_1 \cdot \boldsymbol{\tau}_2]$, of the full two-body potential, constructed to preserve the potential in all S and P waves as well as the $^3\mathrm{D}_1$ and its coupling to the $^3\mathrm{S}_1$.

The desired expectation values of ground-state and low-lying excited-state observables are then computed approximately by stochastic integration of mixed matrix elements [73]

$$\langle \mathcal{O}(\tau) \rangle_{\mathrm{M}} = \frac{\langle \Psi(\tau) | \mathcal{O} | \Psi_T \rangle}{\langle \Psi(\tau) | \Psi_T \rangle}, \tag{17}$$

where $\mathcal{O}$ is the observable of interest to be evaluated. By writing $\Psi(\tau) = \Psi_T + \delta\Psi(\tau)$ and neglecting terms of order $[\delta\Psi(\tau)]^2$, one obtains an approximate expression for

$$\langle \mathcal{O}(\tau) \rangle \equiv \frac{\langle \Psi(\tau) | \mathcal{O} | \Psi(\tau) \rangle}{\langle \Psi(\tau) | \Psi(\tau) \rangle} \approx \langle \mathcal{O}(\tau) \rangle_{\mathrm{M}} + [\langle \mathcal{O}(\tau) \rangle_{\mathrm{M}} - \langle \mathcal{O} \rangle_{\mathrm{V}}], \tag{18}$$

where $\langle \mathcal{O} \rangle_{\mathrm{V}}$ is the variational expectation value.

In the case of the Hamiltonian, since the propagator commutes with it, the mixed estimate $\langle H(\tau) \rangle_{\mathrm{M}}$ of Eq. (17) is itself an upper bound to the the ground-state energy $E_0$ and can be expressed as [73]

$$E(\tau) = \langle H(\tau) \rangle_{\mathrm{M}} = \frac{\langle \Psi(\tau/2) | H | \Psi(\tau/2) \rangle}{\langle \Psi(\tau/2) | \Psi(\tau/2) \rangle}. \tag{19}$$

Because the simpler $H'$ is used to generate the GFMC propagator the total energy is then computed by the mixed estimate of $H'$ plus the difference $\langle H - H' \rangle_{\mathrm{M}}$ evaluated by Eq. (18).

Apart from the use of mixed estimates and $H'$ in the propagation, another source of systematic errors that affects GFMC calculations is the well-known fermion sign problem. In essence this results from the fact that during the imaginary-time propagation bosonic noise gets mixed into the propagated wave function. This bosonic component has a much lower energy than the fermion component and thus is exponentially amplified in subsequent iterations of the short-time propagators. The desired fermionic component is projected out by the antisymmetric $\Psi_T$ when Eq. (17) is evaluated; however, the presence of large statistical errors which increase with $\tau$ effectively limits the maximum $\tau$ that can be used in the calculations. Since the number of pairs to be exchanged grows with the mass number $A$, the sign problem also grows exponentially with increasing $A$.

For spin- and isospin-dependent wave functions, the fermion sign problem can be controlled by a suitable constrained path approximation, which basically limits the propagation to regions where the propagated $|\Psi(\tau)\rangle$ and trial $|\Psi_T\rangle$ wave functions have a positive overlap and discards those configurations that instead have a negative or vanishing overlap (see Ref. [74] for details on this topic). To address the possible bias that the constrained path technique can introduce in the

TABLE VI. The $^3$H ground-state energies $E_0$ (MeV) and rms proton radii $r_p$ (fm) with models $a$, $\widetilde{a}$, $b$, and $\widetilde{b}$. Statistical errors on the energy evaluations are indicated in parentheses for the VMC and GFMC calculations.

| Method | Model $a$ | | Model $\widetilde{a}$ | | Model $b$ | | Model $\widetilde{b}$ | |
|---|---|---|---|---|---|---|---|---|
| | $E_0$ | $\sqrt{\langle r_p^2\rangle}$ | $E_0$ | $\sqrt{\langle r_p^2\rangle}$ | $E_0$ | $\sqrt{\langle r_p^2\rangle}$ | $E_0$ | $\sqrt{\langle r_p^2\rangle}$ |
| VMC | –7.592(6) | 1.65 | –7.691(6) | 1.62 | –7.317(7) | 1.68 | –7.643(5) | 1.63 |
| GFMC | –7.818(8) | 1.62 | –7.917(10) | 1.60 | –7.627(17) | 1.65 | –7.863(8) | 1.57 |
| HH | –7.818 | | –7.949 | | –7.599 | | –7.866 | |

calculations, all the configurations, including those that are being rejected, for the previous $n_{\rm uc}$ (typical $10-20$) time steps are used when evaluating expectation values. In general the number $n_{\rm uc}$ is chosen to be as large as possible within a reasonable statistical error.

For phenomenological nuclear Hamiltonians (such those based on the AV18 potential) the constrained-path approximation was not necessary for calculations of $A \leqslant 4$ systems, since the sign problem was quite mild for these light nuclei. On the other hand, it is essential for GFMC calculations with the N(3)LO *NN* chiral interactions of Sec. II, since the sign problem is far more severe for this category of potentials.

### C. Results for binding energies

In this section we present results for ground and excited states of $^3$H, $^3$He, $^4$He, $^6$He, and $^6$Li nuclei using a subset of the local chiral potentials discussed in Sec. II. In particular, in order to solve the $^3$H and $^4$He ground states, we use VMC, GFMC, and HH methods with N(3)LO *NN* models $a$, $\widetilde{a}$, $b$, and $\widetilde{b}$, while for $^3$He, $^6$He, and $^6$Li ground and excited states we present VMC and GFMC calculations performed with model $\widetilde{b}$ only.

The variational wave functions used for the VMC results include only spatial and spin-isospin two-body correlations denoted by $U_{ij}$ as in Refs. [70,73]; the Jastrow wave functions for the $s$-shell ($A=3$ and 4) and $p$-shell ($A=6$) nuclei are also given explicitly in those references. For these calculations, the search in parameter space is made using COBYLA (Constrained Optimization BY Linear Approximations) algorithm available in the NLopt [75] library. The optimal parameters are found typically using runs of 100 000 configurations for the evaluation of matrix elements in Eq. (14). When the optimal trial wave function is found, a long run with 1 000 000, 500 000, and 200 000 configurations is made in $A=3$, 4, and 6 nuclei, respectively, which then is used as input for the GFMC calculations. The GFMC results are obtained using the constrained path technique with $n_{\rm uc}=20$ unconstrained time steps. The imaginary-time evolution for the $a$ and $\widetilde{b}$ models ($\widetilde{a}$ and $b$ ones) is computed with small time step $\Delta\tau = 0.0005\,(0.0001)\,{\rm MeV}^{-1}$ up to total time $\tau = 0.2\,{\rm MeV}^{-1}$.

The results for the $^3$H and $^4$He ground states are shown in Tables VI and VII, respectively. The VMC calculations give energies that are 3–4% above the corresponding HH or GFMC predictions; the latter are in good agreement with each other. The errors quoted for the VMC and GFMC results are the Monte Carlo statistical errors. We see that increasing the laboratory energy range, in which the LECs are fitted, from 125 to 200 MeV (as discussed in Sec. III), leads to more binding for these systems.

In Table VIII we present the GFMC calculations for the $^3$H and $^4$He ground-state energies and rms proton radii at LO, NLO, N2LO, and N(3)LO in the chiral expansion for potential model $b$. At LO we find that the nuclei are significantly overbound by as much as 5 MeV (for $^3$H) and 27 MeV (for $^4$He) over their corresponding experimental values, $E_0 = -8.482$ MeV (for $^3$H) and $E_0 = -28.30$ MeV (for $^4$He). The NLO contribution is an important correction to the LO results. At this order the $^3$H and $^4$He become, respectively, $\sim$1 and $\sim$5 MeV underbound compared to their experimental values. At N2LO and N(3)LO the nuclei are still underbound, but getting closer to experimental results. The N2LO contributions are small relative to the NLO ones and the N(3)LO corrections to the N2LO results are almost negligible within the statistical errors.

In Table IX we report VMC and GFMC calculations for $^3$H, $^3$He, $^4$He, $^6$He, and $^6$Li ground and excited states obtained using model $\widetilde{b}$, which has, among the N(3)LO local potentials presented in Sec. II, the best behavior in terms of sign problem. In that table we also report the corresponding GFMC calculation obtained with the AV18. We note that for $A=3$, 4 and 6 the binding energies obtained using model $\widetilde{b}$ differ by about 0.2 – 0.3, 1.07, and 1.3 – 0.5 MeV, respectively, from the corresponding ones obtained using AV18.

The optimization of the $^3$He ground state has been performed using as starting point the variational parameters for

TABLE VII. Same as in Table VI but for the $^4$He ground state.

| Method | Model $a$ | | Model $\widetilde{a}$ | | Model $b$ | | Model $\widetilde{b}$ | |
|---|---|---|---|---|---|---|---|---|
| | $E_0$ | $\sqrt{\langle r_p^2\rangle}$ | $E_0$ | $\sqrt{\langle r_p^2\rangle}$ | $E_0$ | $\sqrt{\langle r_p^2\rangle}$ | $E_0$ | $\sqrt{\langle r_p^2\rangle}$ |
| VMC | –24.38(1) | 1.51 | –25.03(1) | 1.49 | –22.89(2) | 1.54 | –24.46(2) | 1.49 |
| GFMC | –25.13(5) | 1.49 | –25.71(3) | 1.50 | –23.88(5) | 1.53 | –25.21(4) | 1.45 |
| HH | –25.15 | | –25.80 | | –23.96 | | –25.28 | |

TABLE VIII. GFMC calculations order by order in the chiral expansion for $^3$H and $^4$He ground-state energies $E_0$ (MeV) and rms proton radii $r_p$ (fm) obtained using model $b$. Statistical errors on the energy evaluations are indicated in parentheses. The experimental binding energy and rms proton radius are $E_0 = -8.482$ MeV and $\sqrt{\langle r_p^2\rangle} = 1.58$ fm for $^3$H [13] and $E_0 = -28.30$ MeV and $\sqrt{\langle r_p^2\rangle} = 1.462$ fm for $^4$He [13].

| Model | Order | $^3$H | | $^4$He | |
|---|---|---|---|---|---|
| | | $E_0$ | $\sqrt{\langle r_p^2\rangle}$ | $E_0$ | $\sqrt{\langle r_p^2\rangle}$ |
| $b$ | LO | –13.407(9) | 1.23 | –55.53(1) | 0.90 |
| $b$ | NLO | –7.379(4) | 1.69 | –23.04(2) | 1.55 |
| $b$ | N2LO | –7.574(9) | 1.65 | –23.95(3) | 1.52 |
| $b$ | N(3)LO | –7.627(17) | 1.65 | –23.88(5) | 1.53 |

$^3$H, but varying only the separation energies and tensor/central ratios—these parameters characterize the asymptotic boundary conditions imposed on the pair-correlation functions [70]. The calculated VMC energy, as shown in Table IX, is ∼0.2 MeV above the GFMC one.

The ground state of $^6$He, not bound with respect to the $^4$He threshold with model $\widetilde{b}$ or AV18, is a $(J^\pi, T) = (0^+; 1)$ state which has predominantly a $^{2S+1}\mathrm{L}[n] = {}^1\mathrm{S}[42]$ character (we use spectroscopic notation to denote the orbital angular momentum $L$, the spin $S$, and the Young diagram spatial symmetry $[n]$ of the state). The $(2^+; 1)$ first excited state, mostly a $^1D[42]$ state, is above the threshold for decay to $\alpha + 2n$ with a width of ≈100 keV and we treat it as a stable state. For both states we allow a possible $^3P[411]$ admixture in the total wave function, and then use generalized eigenvalue routines to diagonalize the resulting $2 \times 2$ matrix for each of them and extract the corresponding contributions, $^1S[42]$ and $^3P[411]$ for the $(0^+; 1)$ ground state, and $^1D[42]$ and $^3P[411]$ for the $(2^+; 1)$ excited state. We do not report the calculated energies for the three $^3P[411]$ states with $(J^\pi, T) = (2^+; 1)$, $(1^+; 1)$, and $(0^+; 1)$ since they have yet to be identified experimentally.

The $p$-shell spectrum for $^6$Li consists of a $(1^+; 0)$ ground state, which is mostly a $^3S[42]$ state, a triplet of $^3D[42]$ excited states with $(3^+; 0)$, $(2^+; 0)$, and $(1^+; 0)$ components, and a singlet of $^1P[411]$ excited state with a $(1^+; 0)$ component, the latter not yet identified experimentally. The $^6$Li ground state is stable while the excited states are above the $\alpha + d$ threshold, but we treat them as bound states here. In addition there are $(0^+; 1)$ and $(2^+; 1)$ excited states that are the isobaric analogs of the $^6$He states, but they will not be discussed here. For the $(1^+; 0)$ ground and excited states we allow admixtures of $^3S[42]$, $^3D[42]$, and $^1P[411]$ components in the total wave function and then diagonalize a $3 \times 3$ matrix to extract the corresponding contributions. This diagonalization procedure is not necessary for the $(3^+; 0)$ and $(2^+; 0)$ excited states since both of them are pure $^3D[42]$ states. The energies of the $^3D[42]$ triplet give a measure of the effective one-body spin-orbit splitting. The $J$-averaged centroids for both model $\widetilde{b}$ and AV18 are 3.6 MeV above their respective ground states; however, the spread between lowest and highest triplet members is 1.5 MeV for model $\widetilde{b}$ and 2.1 MeV for AV18.

The minimization of the energy for the $^6$Li ground state has been carried out by requiring the resulting proton rms radius, $r_p$, to be close to the GFMC one obtained with the AV18. For the excited states, we minimize their energies by requiring that these excited states have radii only slightly larger than the ground state. A similar optimization strategy has been adopted for the $^6$He ground and excited states, except that we use as starting point the $^6$Li variational parameters and vary only those parameters associated with the single-particle radial functions, $\phi_p$, in the Jastrow part of the trial wave function [73].

## V. SUMMARY AND CONCLUSIONS

In the present work we have constructed two classes of chiral potentials at N(3)LO, which are fully local in configuration space, for use (primarily) with HH and QMC methods. The two classes only differ in the range of laboratory energies over which the LECs in the contact interactions have been fitted to the *NN* database (as assembled by the Granada group), either 0- to 125-MeV (models $a$, $b$, and $c$) with $\chi^2$/datum $\lesssim 1.1$ for a total of about 2700 data points or 0- to 200-MeV (models $\widetilde{a}$, $\widetilde{b}$, and $\widetilde{c}$) with $\chi^2$/datum $\lesssim 1.4$ for about 3700 data points (representing an increase of roughly 40% in the size of the fitted database relative to the 0- to 125-MeV case). Within a

TABLE IX. The $^3$H, $^3$He, $^4$He, $^6$He, and $^6$Li ground- and excited-state energies in MeV and proton rms radii $r_p$ in fm with model $\widetilde{b}$ compared with the corresponding GFMC results obtained with the AV18. Statistical errors on the energy evaluations are indicated in parentheses.

| $^A Z(J^\pi; T)$ | VMC | | GFMC | | GFMC(AV18) | |
|---|---|---|---|---|---|---|
| | $E_0$ | $\sqrt{\langle r_p^2\rangle}$ | $E_0$ | $\sqrt{\langle r_p^2\rangle}$ | $E_0$ | $\sqrt{\langle r_p^2\rangle}$ |
| $^3\mathrm{H}(\frac{1}{2}^+; \frac{1}{2})$ | –7.643(5) | 1.63 | –7.863(8) | 1.57 | –7.610(5) | 1.66 |
| $^3\mathrm{He}(\frac{1}{2}^+; \frac{1}{2})$ | –6.907(5) | 1.84 | –7.115(9) | 1.84 | –6.880(5) | 1.85 |
| $^4\mathrm{He}(0^+; 0)$ | –24.46(2) | 1.49 | –25.21(4) | 1.45 | –24.14(1) | 1.49 |
| $^6\mathrm{He}(0^+; 1)$ | –22.58(3) | 2.05 | –24.53(6) | 2.07(1) | –23.76(9) | 2.06(1) |
| $^6\mathrm{He}(2^+; 1)$ | –20.94(2) | 2.06 | –22.87(6) | 2.18(2) | –21.85(9) | 2.11(1) |
| $^6\mathrm{Li}(1^+; 0)$ | –25.86(3) | 2.58 | –27.71(8) | 2.62(1) | –26.87(9) | 2.58(1) |
| $^6\mathrm{Li}(3^+; 0)$ | –22.73(3) | 2.59 | –24.56(8) | 2.59(1) | –24.11(7) | 2.87(1) |
| $^6\mathrm{Li}(2^+; 0)$ | –21.42(3) | 2.61 | –24.04(9) | 2.79(2) | –22.75(11) | 2.63(1) |
| $^6\mathrm{Li}(1_2^+; 0)$ | –20.42(3) | 2.58 | –23.09(11) | 2.89(2) | –21.99(12) | 2.85(3) |

given class, models $a$, $b$, and $c$ (or $\widetilde{a}$, $\widetilde{b}$, and $\widetilde{c}$) have different short-range and long-range cutoff radii, respectively $R_{\rm L}$ and $R_{\rm S}$: $(R_{\rm L}, R_{\rm S}) = (1.2, 0.8)$ fm for models $a$ and $\widetilde{a}$, (1.0,0.7) fm for models $b$ and $\widetilde{b}$, and (0.8,0.6) fm for models $c$ and $\widetilde{c}$. The cutoff radius $R_{\rm L}$ regularizes the long-range part of the potential, which includes OPE and TPE terms without and with excitation of intermediate Δ isobars as illustrated in Fig. 1 of Ref. [51]. The cutoff radius $R_{\rm S}$ provides a range to the $\delta$ functions and their derivatives, which characterize the contact interactions in the short-range part of the potential. These contact interactions require a total of 26 independent LECs, 20 of which occur in the charge-independent (CI) component and 6 in the charge-dependent (CD) one (5 for central, tensor, and spin-orbit CIB terms, and 1 for a central CSB term). These 26 LECs are then constrained by the fits above (their values are listed in Tables II and III).

A subset of the potentials—$a$, $\widetilde{a}$, $b$, and $\widetilde{b}$—have been used in HH, VMC, and GFMC calculations of binding energies and proton rms radii of nuclei with $A = 2$–6. The GFMC calculations are rather challenging owing to the serious fermion-sign problem associated with these potentials, even for $s$-shell nuclei ($^3$H, $^3$He, and $^4$He); this problem becomes especially severe for models $c$ and $\widetilde{c}$, and they have not been used in the present work. However, implementation of the constrained-path algorithm in the course of the imaginary-time propagation substantially reduces the statistical fluctuations in the energy evaluation, and leads to $^3$H and $^3$He ground-state energies in excellent agreement with those obtained in the HH calculations. All present models, especially $c$ and $\widetilde{c}$, have rather strong spin-orbit, quadratic orbital angular momentum ($\mathbf{L}^2$), and quadratic spin-orbit components, particularly in the $(S,T) = (1,0)$ channel: For internucleon separation close to zero, they have values of ∼2800 MeV, ∼200 MeV, and ∼460 MeV respectively, in this channel. While these components vanish for nucleon pairs in relative $S$ wave, they do so, in the course of a GFMC imaginary-time propagation, only by averaging large values of opposite signs, thus producing large fluctuations.

The models $\widetilde{a}$ and $\widetilde{b}$ produce more binding in $A = 3$ and 4 nuclei than $a$ and $b$; the extra binding of model $\widetilde{b}$ relative to $b$ amounts to 5% in $^4$He. It appears that model $\widetilde{b}$ leads to ground- and excited-state energies of $A = 3$–6 nuclei, which are close to those calculated with AV18. Clearly, the next stage in the program of studies of light nuclei structure with chiral interactions we envision is the inclusion of a three-nucleon potential. A chiral version of it at leading order, including Δ-isobar intermediate states, has been developed, and is currently being constrained by reproducing observables in the $A = 3$ systems.

We conclude by observing that a number of different groups [76–78] have developed procedures which allow us to assess, in a systematic way, the theoretical uncertainties inherent to the use of chiral potentials. In the present work these uncertainties have been estimated by investigating (i) how the $\chi^2$/datum and $^3$H and $^4$He binding energies change as the long- and short-range cutoffs are varied, (ii) how these $\chi^2$/datum and binding energy values change as the range of laboratory energy used in constraining the fits is extended from 125 to 200 MeV, and (iii) how for a fixed set of cutoffs (those of model $b$) the quality of the fit and the $^3$H and $^4$He ground-state energies improves with increasing order in the chiral expansion.

## ACKNOWLEDGMENTS

Conversations and e-mail exchanges with J. Carlson and S. Gandolfi are gratefully acknowledged. The work of M.P., A.L., S.C.P., and R.B.W. has been supported by the NUclear Computational Low-Energy Initiative (NUCLEI) SciDAC project. This research is supported by the US Department of Energy, Office of Science, Office of Nuclear Physics, under Contracts No. DE-AC02-06CH11357 (M.P., A.L., S.C.P., and R.B.W.) and No. DE-AC05-06OR23177 (R.S.). This research also used resources provided by Argonne's Laboratory Computing Resource Center and the National Energy Research Scientific Computing Center (NERSC).

[1] B. R. Barrett, P. Navrtil, and J. P. Vary, Prog. Part. Nucl. Phys. **69**, 131 (2013).
[2] E. D. Jurgenson, P. Maris, R. J. Furnstahl, P. Navrátil, W. E. Ormand, and J. P. Vary, Phys. Rev. C **87**, 054312 (2013).
[3] G. Hagen, T. Papenbrock, A. Ekström, K. A. Wendt, G. Baardsen, S. Gandolfi, M. Hjorth-Jensen, and C. J. Horowitz, Phys. Rev. C **89**, 014319 (2014).
[4] G. Hagen, T. Papenbrock, M. Hjorth-Jensen, and D. J. Dean, Rep. Prog. Phys. **77**, 096302 (2014).
[5] M. Viviani, L. E. Marcucci, S. Rosati, A. Kievsky, and L. Girlanda, Few-Body Syst. **39**, 159 (2006).
[6] L. E. Marcucci, A. Kievsky, L. Girlanda, S. Rosati, and M. Viviani, Phys. Rev. C **80**, 034003 (2009).
[7] M. Viviani, A. Kievsky, L. Girlanda, L. E. Marcucci, and S. Rosati, Few-Body Syst. **45**, 119 (2009).
[8] M. Viviani, L. Girlanda, A. Kievsky, L. E. Marcucci, and S. Rosati, EPJ Web Conf. **3**, 05011 (2010).
[9] S. Bogner, R. Furnstahl, and A. Schwenk, Prog. Part. Nucl. Phys. **65**, 94 (2010).
[10] H. Hergert, S. K. Bogner, S. Binder, A. Calci, J. Langhammer, R. Roth, and A. Schwenk, Phys. Rev. C **87**, 034307 (2013).
[11] W. Dickhoff and C. Barbieri, Prog. Part. Nucl. Phys. **52**, 377 (2004).
[12] V. Somà, C. Barbieri, and T. Duguet, Phys. Rev. C **87**, 011303 (2013).
[13] J. Carlson *et al.*, Rev. Mod. Phys. **87**, 1067 (2015).
[14] S. Weinberg, Phys. Lett. B **251**, 288 (1990); Nucl. Phys. B **363**, 3 (1991); Phys. Lett. B **295**, 114 (1992).
[15] E. Epelbaum, H. W. Hammer, and U.-G. Meißner, Rev. Mod. Phys. **81**, 1773 (2009).
[16] R. Machleidt and D. R. Entem, Phys. Rep. **503**, 1 (2011).
[17] N. Kalantar-Nayestanaki *et al.*, Rept. Prog. Phys. **75**, 016301 (2012).
[18] H. W. Hammer, A. Nogga, and A. Schwenk, Rev. Mod. Phys. **85**, 197 (2013).
[19] N. Kaiser, R. Brockmann, and W. Weise, Nucl. Phys. A **625**, 758 (1997).

[20] N. Kaiser, S. Gerstendörfer, and W. Weise, Nucl. Phys. A **637**, 395 (1998).
[21] N. Kaiser, Phys. Rev. C **61**, 014003 (1999).
[22] N. Kaiser, Phys. Rev. C **62**, 024001 (2000).
[23] N. Kaiser, Phys. Rev. C **63**, 044010 (2001).
[24] N. Kaiser, Phys. Rev. C **64**, 057001 (2001).
[25] N. Kaiser, Phys. Rev. C **65**, 017001 (2001).
[26] E. Epelbaum, W. Glöckle, and U.-G. Meißner, Nucl. Phys. A **637**, 107 (1998); **671**, 295 (2000).
[27] D. R. Entem and R. Machleidt, Phys. Rev. C **66**, 014002 (2002).
[28] H. Krebs, E. Epelbaum, and U.-G. Meißner, Eur. Phys. J. A **32**, 127 (2007).
[29] D. R. Entem and R. Machleidt, Phys. Rev. C **68**, 041001(R) (2003).
[30] E. Epelbaum, W. Glöckle, and U.-G. Meißner, Nucl. Phys. A **747**, 362 (2005).
[31] D. Siemens, V. Bernard, E. Epelbaum, A. Gasparyan, H. Krebs, and U.-G. Meißner, Phys. Rev. C **94**, 014620 (2016).
[32] D.-L. Yao, D. Siemens, V. Bernard, E. Epelbaum, A. M. Gasparyan, J. Gegelia, H. Krebs, and U.-G. Meißner, J. High Energy Phys. 05 (2016) 038.
[33] J. M. Alarcón, J. Martin Camalich, and J. A. Oller, Annals Phys. **336**, 413 (2013).
[34] D. R. Entem, N. Kaiser, R. Machleidt, and Y. Nosyk, Phys. Rev. C **91**, 014002 (2015).
[35] E. Epelbaum, H. Krebs, and U.-G. Meißner, Phys. Rev. Lett. **115**, 122301 (2015).
[36] D. R. Entem, N. Kaiser, R. Machleidt, and Y. Nosyk, Phys. Rev. C **92**, 064001 (2015).
[37] V. G. J. Stoks, R. A. M. Klomp, M. C. M. Rentmeester, and J. J. de Swart, Phys. Rev. C **48**, 792 (1993).
[38] V. G. J. Stoks, R. A. M. Klomp, C. P. F. Terheggen, and J. J. de Swart, Phys. Rev. C **49**, 2950 (1994).
[39] R. A. Arndt, I. I. Strakovsky, and R. L. Workman, SAID, Scattering Analysis Interactive Dial-in computer facility, George Washington University, solution SM99 (Summer 1999) (unpublished).
[40] R. N. Pérez, J. E. Amaro, and E. R. Arriola, Phys. Rev. C **88**, 064002 (2013); **89**, 024004 (2014); **89**, 064006 (2014).
[41] A. Ekström, G. R. Jansen, K. A. Wendt, G. Hagen, T. Papenbrock, B. D. Carlsson, C. Forssén, M. Hjorth-Jensen, P. Navrátil, and W. Nazarewicz, Phys. Rev. C **91**, 051301(R) (2015).
[42] R. B. Wiringa, V. G. J. Stoks, and R. Schiavilla, Phys. Rev. C **51**, 38 (1995).
[43] J. Carlson, V. R. Pandharipande, and R. B. Wiringa, Nucl. Phys. A **401**, 59 (1983).
[44] B. S. Pudliner, A. Smerzi, J. Carlson, V. R. Pandharipande, S. C. Pieper, and D. G. Ravenhall, Phys. Rev. Lett. **76**, 2416 (1996).
[45] S. C. Pieper, AIP Conf. Proc. **1011**, 143 (2008).
[46] S. C. Pieper, V. R. Pandharipande, R. B. Wiringa, and J. Carlson, Phys. Rev. C **64**, 014001 (2001).
[47] A. Gezerlis, I. Tews, E. Epelbaum, S. Gandolfi, K. Hebeler, A. Nogga, and A. Schwenk, Phys. Rev. Lett. **111**, 032501 (2013).
[48] A. Gezerlis, I. Tews, E. Epelbaum, M. Freunek, S. Gandolfi, K. Hebeler, A. Nogga, and A. Schwenk, Phys. Rev. C **90**, 054323 (2014).
[49] J. E. Lynn, J. Carlson, E. Epelbaum, S. Gandolfi, A. Gezerlis, and A. Schwenk, Phys. Rev. Lett. **113**, 192501 (2014).
[50] J. E. Lynn, I. Tews, J. Carlson, S. Gandolfi, A. Gezerlis, K. E. Schmidt, and A. Schwenk, Phys. Rev. Lett. **116**, 062501 (2016).
[51] M. Piarulli, L. Girlanda, R. Schiavilla, R. N. Pérez, J. E. Amaro, and E. R. Arriola, Phys. Rev. C **91**, 024003 (2015).
[52] B. Long and V. Lensky, Phys. Rev. C **83**, 045206 (2011).
[53] M. Kortelainen, T. Lesinski, J. Moré, W. Nazarewicz, J. Sarich, N. Schunck, M. V. Stoitsov, and S. Wild, Phys. Rev. C **82**, 024313 (2010).
[54] F. L. Gross and A. Stadler, Phys. Rev. C **78**, 014005 (2008).
[55] J. R. Bergervoet, P. C. van Campen, W. A. van der Sanden, and J. J. de Swart, Phys. Rev. C **38**, 15 (1988).
[56] W. A. van der Sanden, A. H. Emmen, and J. J. de Swart, Report No. THEF-NYM-83.11, Nijmegen, 1983 (unpublished); quoted in Ref. [55].
[57] Q. Chen, C. R. Howell, T. S. Carman, W. R. Gibbs, B. F. Gibson, A. Hussein, M. R. Kiser, G. Mertens, C. F. Moore, C. Morris, A. Obst, E. Pasyuk, C. D. Roper, F. Salinas, H. R. Setze, I. Slaus, S. Sterbenz, W. Tornow, R. L. Walter, C. R. Whiteley, and M. Whitton, Phys. Rev. C **77**, 054002 (2008).
[58] G. A. Miller, M. K. Nefkens, and I. Slaus, Phys. Rep. **194**, 1 (1990).
[59] R. Machleidt, Phys. Rev. C **63**, 024001 (2001).
[60] T. E. O. Ericson and M. Rosa-Clot, Nucl. Phys. A **405**, 497 (1983).
[61] N. L. Rodning and L. D. Knutson, Phys. Rev. C **41**, 898 (1990).
[62] A. Huber, T. Udem, B. Gross, J. Reichert, M. Kourogi, K. Pachucki, M. Weitz, and T. W. Hansch, Phys. Rev. Lett. **80**, 468 (1998).
[63] J. Martorell, D. W. L. Sprung, and D. C. Zheng, Phys. Rev. C **51**, 1127 (1995).
[64] M. Piarulli, L. Girlanda, L. E. Marcucci, S. Pastore, R. Schiavilla, and M. Viviani, Phys. Rev. C **87**, 014006 (2013).
[65] A. Kievsky, M. Viviani, and S. Rosati, Nucl. Phys. A **577**, 511 (1994).
[66] A. Kievsky, L. E. Marcucci, S. Rosati, and M. Viviani, Few-Body Syst. **22**, 1 (1997).
[67] M. Viviani, A. Kievsky, and S. Rosati, Phys. Rev. C **71**, 024006 (2005).
[68] A. Kievsky, S. Rosati, M. Viviani, L. E. Marcucci, and L. Girlanda, J. Phys. G: Nucl. Part. Phys. **35**, 063101 (2008).
[69] N. Metropolis, A. W. Rosenbluth, M. N. Rosenbluth, A. H. Teller, and E. Teller, J. Chem. Phys. **21**, 1087 (1953).
[70] R. B. Wiringa, Phys. Rev. C **43**, 1585 (1991).
[71] J. Carlson, Phys. Rev. C **36**, 2026 (1987).
[72] J. Carlson, Phys. Rev. C **38**, 1879 (1988).
[73] B. S. Pudliner, V. R. Pandharipande, J. Carlson, S. C. Pieper, and R. B. Wiringa, Phys. Rev. C **56**, 1720 (1997).
[74] R. B. Wiringa, S. C. Pieper, J. Carlson, and V. R. Pandharipande, Phys. Rev. C **62**, 014001 (2000).
[75] http://ab-initio.mit.edu/wiki/index.php/NLopt.
[76] E. Epelbaum, H. Krebs, and U.-G. Meissner, Eur. Phys. J. A **51**, 53 (2015).
[77] S. Wesolowski, N. Klco, R. J. Furnstahl, D. R. Phillips, and A. Thapaliya, J. Phys. G **43**, 074001 (2016).
[78] B. D. Carlsson, A. Ekstrom, C. Forssen, D. F. Strömberg, G. R. Jansen, O. Lilja, M. Lindby, B. A. Mattsson, and K. A. Wendt, Phys. Rev. X **6**, 011019 (2016).